HHS Public Access

Author manuscript

*Magn Reson Med*. Author manuscript; available in PMC 2023 January 01.

Published in final edited form as:

*Magn Reson Med*. 2022 March ; 87(3): 1418–1434. doi:10.1002/mrm.29063.

# Optimization of spin-lock times in $T_{1\rho}$ mapping of knee cartilage: Cramér-Rao bounds versus matched sampling-fitting

**Marcelo V W Zibetti**[1], **Azadeh Sharafi**[1], **Ravinder R Regatte**[1]

[1]Center for Biomedical Imaging, Department of Radiology, New York University School of Medicine, New York, NY, USA

## Abstract

**Purpose:** To compare different optimization approaches for choosing the spin-lock times (TSLs), in spin-lattice relaxation time in the rotating frame ($T_{1\rho}$) mapping.

**Methods:** Optimization criteria for TSLs based on Cramér-Rao lower bounds (CRLB) are compared with matched sampling-fitting (MSF) approaches for $T_{1\rho}$ mapping on synthetic data, model phantoms, and knee cartilage. The MSF approaches are optimized using robust methods for noisy cost functions. The MSF approaches assume that optimal TSLs depend on the chosen fitting method. An iterative non-linear least squares (NLS) and artificial neural networks (ANN) are tested as two possible $T_{1\rho}$ fitting methods for MSF approaches.

**Results:** All optimized criteria were better than non-optimized ones. However, we observe that a modified CRLB and an MSF based on the mean of the normalized absolute error (MNAE) were more robust optimization approaches, performing well in all tested cases. The optimized TSLs obtained the best performance with synthetic data (3.5–8.0% error), model phantoms (1.5–2.8% error), and healthy volunteers (7.7–21.1% error), showing stable and improved quality results, comparing to non-optimized approaches (4.2–13.3% error on synthetic data, 2.1–6.2% error on model phantoms, 9.8–27.8% error on healthy volunteers).

**Conclusion:** A modified CRLB and the MSF based on MNAE are robust optimization approaches for choosing TSLs in $T_{1\rho}$ mapping. All optimized criteria allowed good results even using rapid scans with 2 TSLs when a complex-valued fitting is done with iterative NLS or ANN.

### Keywords

$T_{1\rho}$ relaxation; Cramér-Rao bounds; spin-lock times; quantitative MRI

## 1. INTRODUCTION

The spin-lattice relaxation time in the rotating frame ($T_{1\rho}$) has shown sensitiveness to loss of proteoglycan content in the cartilage (1,2) and $T_{1\rho}$ relaxation mapping can be useful for early detection of osteoarthritis (OA) (3). To produce good and stable $T_{1\rho}$ maps, many $T_{1\rho}$-

Corresponding Author: **Marcelo V W Zibetti**, Center for Biomedical Imaging, Department of Radiology, New York University School of Medicine, 660 1st Avenue, 4th floor. New York, NY, 10016, USA, marcelo.zibetti@nyumc.org, tel: +1-646-501-9638, fax: +1.

weighted images must be acquired, taking a long acquisition time if a good signal-to-noise ratio (SNR) and small variance in the estimated parameters are desired.

The quality of $T_{1\rho}$ mapping can be improved if the SNR of the acquired data is improved (4). This can be achieved by using different pulse sequences (5), by averaging multiple acquisitions, or even by using multiple receiving coils (6). Specifically, in $T_{1\rho}$ mapping, improved quality can also be obtained by optimally choosing the spin-lock times (TSLs), also called optimal TSL sampling schedules (7). Efficient choices can reduce the overall acquisition time while maintaining a good quality of the estimated parameters.

The choice of the sampling schedules is important in quantitative MRI in general. This has been discussed for $T_{1\rho}$ mapping (7), for spin-lattice relaxation time ($T_1$) and spin-spin relaxation time ($T_2$) mapping (8–12), for magnetic resonance (MR) fingerprinting (13,14). Typically, this problem is handled with optimization of the Cramér-Rao lower bounds (CRLB) (15). Improving the CRLB using better signal sampling is related to the improvement of the stability of unbiased statistical estimators. In (16,17), the similarity in construction of the Fisher information matrix (FIM), used in the CRLB optimizations, and the Hessian matrix (or its approximations using the Jacobian matrix), used by fitting algorithms based on non-linear least squares (NLS) (18), is demonstrated for the case of Gaussian noise and differentiable fitting models. Essentially, this implies that optimizing the sampling schedule using CRLB leads to a “regularization by discretization” of the NLS problem (19), improving the condition number of the matrix used in the non-linear system solved by these algorithms and, consequently, stabilizing the non-linear inverse problem (17). Even though NLS methods had direct benefit from the optimized sampling schedule, other aspects of the estimation algorithms are not considered when using CRLB, such as the type of iterative algorithm, constraints, step-sizes, number of iterations, or initial guess. However, these choices are relevant for the effectiveness of the fitting algorithm. Data-driven approaches, such as those used to optimize the k-space sampling pattern in MRI (20–22) and flip-angles in T1 mapping (16), can consider the specific strategies of a fitting algorithm. These approaches claim that effective sampling patterns depend on the recovering method and expected signal parameters. They are called here as matched sampling-fitting (MSF) because they include the fitting algorithm in their criterion for optimal sampling.

While curve fitting is classically solved with NLS, other approaches, such as artificial neural networks (ANNs)(23–27) can be exploited. Curve fitting with ANNs is not a novelty (23), but the topic has been revived in MRI (28–30) due to the good results of deep learning with relaxometry (31,32). An ANN is usually trained with sample data of the expected exponential relaxation process. The input signals are non-linearly processed by the ANN to obtain the parameters of the relaxation model. Since ANN works differently from unbiased estimators, it is not known if optimization of the sampling schedules with CRLB is useful for $T_{1\rho}$ mapping with ANNs.

Both approaches, CRLB and MSF, consider a specific distribution of relaxation parameters for the optimization process, which should correspond to the distribution expected on the scanned subjects. Besides, there are many possible cost functions to compose a criterion. The cost function objectively defines what the best sampling schedules are (considering

a given distribution of relaxation parameters is expected). All these choices lead to different optimal sampling schedules, which may have different performances in practical applications.

In this study, we compare four different criteria. Two CRLB criteria are compared: one based on the sum of the CRLB for each parameter, and the other one based on the sum of the squared root of the CRLB normalized by its parameter value. Also, two MSF criteria are compared: one based on the mean squared error (MSE), and the other one based on the mean of the normalized absolute error (MNAE). All approaches consider the monoexponential complex-valued signal model, the expected distribution of parameters in the human knee cartilage, and complex-valued Gaussian noise. Besides, MSF criteria also consider the fitting method. Because MSF leads to the optimization of noisy cost functions, we optimize it with subset selection algorithms for noisy problems, such as (33).

We observe that different optimal TSLs are obtained from different criteria and, in general, they are always better than non-optimized TSLs. However, the Modified CRLB and the MSF criterion based on MNAE described later in this work are more robust approaches, being insensitive if the model of choice considers the optimization of $T_{1\rho}$ or its inverse, the spin-lattice relaxation rate in the rotating frame ($R_{1\rho}$). These optimizing approaches obtained TSLs that are stable across the test problems, enabling good $T_{1\rho}$ mapping results for synthetic data, model phantoms, and healthy volunteer's knee cartilage.

## 2. METHODS

### 2.1. 3D-$T_{1\rho}$-Weighted Data Acquisition and Reconstruction

The 3D-$T_{1\rho}$-weighted datasets were acquired with various TSLs (optimized and non-optimized) using a modified 3D Cartesian low flip-angle fast gradient-echo sequence (34). Fourier Transform is applied in the readout (frequency-encoding) direction, denominated $k_x$, to separate 3D Cartesian data into multiple 2D slices on the $k_y$-$k_z$ plane.

The MRI scans were performed using a 3T clinical MRI scanner (Prisma, Siemens Healthcare, Erlangen, Germany) with a 15-channel Tx/Rx knee coil (QED, Cleveland OH). The $T_{1\rho}$ preparation module *P* uses spin-lock frequency=500Hz and TSL defined by the TSL sampling schedule. The 3D imaging module *A* acquires 64 k-space lines (with 256 samples each) of the data matrix per preparation pulse, using a steady-state sequence with TR/TE=7.60ms/3.86ms and flip-angle=8°, and receiver bandwidth=510 Hz/pixel. A longitudinal magnetization restoration module *R* with delay=1000ms is used after the imaging module *A* and before the repetition of the next set of modules *P*-*A*-*R*, which are repeated 128 times to capture a data matrix of size 256×128×64 per TSL. The slice thickness=2mm, the field of view (FOV)=140mm×140mm. This $T_{1\rho}$ pulse sequence is illustrated in Figure 1. Each module *P* takes approximately the TSL (between 1 and 55 ms), each module *A* takes approximately 64×TR=486.4ms, and each module R takes 1000ms. Each shot is composed of one set of modules *P*-*A*-*R* and takes 1.5 sec. The shots are repeated 128 times to collect all k-space data for one specific TSL, taking 3.28 minutes per TSL. The more TSLs are captured, the longer is the total acquisition time.

After separation of 2D slices, each slice is reconstructed with SENSE (35), that minimizes:

$$\widehat{\boldsymbol{x}}_t = \text{argmin}_{x_t} \|\boldsymbol{y}_t - \boldsymbol{F}\boldsymbol{B}\boldsymbol{x}_t\|_2^2, \quad [1]$$

where $\boldsymbol{x}_t$ is a complex-valued vector that represents an image with TSL $t$, with size $N_y \times N_z = 128 \times 64$, with $N_y$ being the image size in the y-axis and $N_z$ the size in the z-axis. The vector $\boldsymbol{y}_t$ represents the captured k-space with size $N_y \times N_z \times N_c$, where $N_c = 15$ is the number of coils. The matrix $\boldsymbol{B}$ contains the coil sensitivities and phase compensation (36,37), $\boldsymbol{F}$ the Fourier transforms of all sensitivity-weighted images. The $\|\boldsymbol{e}\|_2^2$ is the squared $l_2$-norm or Euclidean norm of $\boldsymbol{e} = \boldsymbol{y}_t - \boldsymbol{F}\boldsymbol{B}\boldsymbol{x}_t$.

The $T_{1\rho}$ magnetization-preparation pulses in this study accept TSLs between 1 and 55 ms, spaced by 1 ms. In this study, two non-optimized choices of TSL, one logarithmically spaced and one linearly spaced within the range of possible TSLs were used to compare against optimized TSLs.

The $T_{1\rho}$-weighted scans were performed in model phantoms and human volunteers. The model phantoms are composed of 2%, 3%, 4%, 5%, and 6% agar gel. The human knee data were acquired in the sagittal plane from five healthy volunteers (males, mean age 31±8 years). Each scanning session acquired 16 TLSs for agar gel model phantoms and 15 TSLs for healthy volunteers, with an acquisition time of 3.28 minutes per TSL. The scanning session of model agar gel phantoms and one human volunteer was repeated for repeatability evaluation. This study was approved by the institutional review board (IRB) and all the volunteers consented before scanning.

## 2.2. Exponential Models:

The $T_{1\rho}$ relaxation is represented using a complex-valued exponentially decaying process (38), described as:

$$x(t, \boldsymbol{n}) = \theta_1(\boldsymbol{n}) exp\left(-\frac{t}{\theta_2(\boldsymbol{n})}\right) + \eta(t, \boldsymbol{n}) \quad [2]$$

with complex-valued $\theta_1(\boldsymbol{n})$, real-valued relaxation time $\theta_2(\boldsymbol{n})$, and complex-valued white Gaussian noise $\eta(t, \boldsymbol{n})$ at spin-lock time $t$ and spatial position $\boldsymbol{n}$ with voxel $[\boldsymbol{x}_t]_{\boldsymbol{n}} = x(t, \boldsymbol{n})$. The model in Equation 2 is the same for all spatial positions, then we will omit $\boldsymbol{n}$ from the following equations. Also, the observed signal will be acquired using $K$ spin-lock times $\boldsymbol{t} = [t_1, \ldots, t_K]^T$, where $t_k \in \mathrm{T}$ which is a finite set containing all possible TSLs one can set in the MRI scanner (between 1 and 55 ms, spaced by 1 ms), $\boldsymbol{x} = [x(t_1), \ldots, x(t_K)]^T$, and the parameters are shown as $\boldsymbol{\theta} = [\theta_1\ \theta_2]^T$. We may write $\boldsymbol{x}(\boldsymbol{t}, \boldsymbol{\theta}) = [x(t_1, \boldsymbol{\theta}), \ldots, x(t_K, \boldsymbol{\theta})]^T$, to emphasize the dependence Equation 2 on the TSL sampling schedule $\boldsymbol{t}$ and parameters $\boldsymbol{\theta}$.

The model based on the $R_{1\rho}$, which is the inverse of the $T_{1\rho}$ value, is described as:

$$x(t_K) = \theta_1 exp\left(-\bar{\theta}_2 t_K\right) + \eta(t_K), \quad [3]$$

where $\bar{\theta}_2 = 1/\theta_2$. Unless explicitly noted, we will use the $T_{1\rho}$ model from Equation 2.

### 2.3. Fitting Algorithms:

Two methods were used for $T_{1\rho}$ fitting. The first method uses NLS, according to:

$$\widehat{\theta} = \arg\min_{\theta \in \boldsymbol{\Theta}} \sum_{k=1}^{K} \left| x(t_k) - f(t_k, \boldsymbol{\theta}) \right|^2 \approx \boldsymbol{R}(\boldsymbol{x}) \quad [4]$$

where $f(t_k, \boldsymbol{\theta}) = \theta_1 \, exp(-t_k/\theta_2)$, and $\boldsymbol{\Theta}$ is a set that contains the relaxation parameters.

Equation 4 is minimized using the conjugate gradient Steihaug's trust-region (CGSTR) algorithm (39), stopping at a maximum of 2500 iterations or when the normalized update is lower than $10^{-9}$. The set $\boldsymbol{\Theta}$ constrains the parameter $\theta_2$, the $T_{1\rho}$ relaxation time, within the range of 10 and 100 ms, while $\theta_1$ is not constrained.

The second fitting method is a shallow ANN (23), with one hidden layer of fully connected components of dimension 12, hyperbolic tangent sigmoid transfer function as the non-linear element, and a linear output layer. The number of inputs is $2K$ where the magnitude and phase of the complex numbers are used as separated inputs for each of the $K$ TSLs. There are 3 real-valued outputs: the magnitude and phase of the $\theta_1$ and the real-valued $\theta_2$. The output $\theta_2$ is constrained between 10 and 100 ms as in the NLS fitting.

To use an ANN for fitting, the following training process needs to be performed:

$$\widehat{\boldsymbol{w}} = \arg\min_{w} \sum_{p=1}^{P} \left\| \boldsymbol{\theta}_p - \boldsymbol{R}(\boldsymbol{w}, \boldsymbol{x}_p) \right\|_2^2 \quad [5]$$

where $\widehat{\theta}_p = \boldsymbol{R}(\boldsymbol{w}, \boldsymbol{x}_p)$ represents the ANN, with parameters $\boldsymbol{w}$ (learned during training) and input signal $\boldsymbol{x}_p$, such as used in (23). The index $p$ is the index of the sample of the parameters $\boldsymbol{\theta} \in \boldsymbol{\Theta}$. The learning problem in Equation 5 is performed using 400 iterations of the Levenberg-Marquadt algorithm (18), using P=20000 samples of the exponential signal $\boldsymbol{x}_p$ artificially generated according to Equation 2. From the parameters $\boldsymbol{\theta}_p = [\theta_1 \; \theta_2]^T$, $\theta_2$ is taken from a uniform distribution between 10 and 100 milliseconds, and the parameter $\theta_1$ is a random complex number with normalized magnitude. The additive Gaussian noise $\eta$ is independent and identically distributed with zero mean and a standard deviation selected to obtain an SNR of 30. The SNR of 30 was the lowest value obtained from measuring SNR in model phantoms and in vivo knee cartilage data, as described next in section 2.4. When the fitting is applied to model phantoms or healthy volunteer data, the signal $\boldsymbol{x}$ is normalized and the normalization constant integrated into parameter $\theta_1$.

### 2.4. $T_{1\rho}$ and SNR Statistics:

For the TSL optimization procedure, it is necessary to give sample values for $\theta_1$, $\theta_2$, and noise. For this purpose, we use reference values from the literature (7) for synthetic experiments and measured values from the model agar gel phantoms and human knee experiments. For synthetic experiments, following (7), we used $T_{1\rho}$ values for $\theta_2$ as a uniform distribution between 20 and 70 ms, $\theta_1$ values as random complex-valued numbers with normalized magnitude, and Gaussian noise with fixed standard deviation to obtain SNR values of 30 and 125 (from our measurements on human volunteers).

For the optimization of the TSLs for model phantoms and knee cartilage, we used data obtained using a non-optimized sequence. First, the noise standard deviation was estimated using the Marchenko–Pastur principal component analysis (MP-PCA) (40). The MP-PCA reshapes the 3D volumes of all $K$ TSLs into a matrix $\boldsymbol{X}$, of size ($K$×256)×(128×64), and uses the singular value decomposition $\boldsymbol{X} = \boldsymbol{U}\boldsymbol{\Lambda}\boldsymbol{V}^T$, with singular values $\{\Lambda_m\}_{m=1}^{M} = diag(\boldsymbol{\Lambda})$. The MP-PCA detects the thresholding $1 \le p \le M$, where the noise standard deviation is

$$\sigma_\eta = \sqrt{\sum_{m=p+1}^{M} \Lambda_m^2/(M-p)}. \quad [6]$$

To obtain values for $\theta_1$ and $\theta_2$, a fitting algorithm was applied voxel-wise in a region of interest (ROI) of the model phantoms and the knee cartilage. The pairs of parameters $\theta_1$ (complex-valued amplitudes) and $\theta_2$ ($T_{1\rho}$ values) were stored. Note that in model phantoms and human knee images, the SNR is variable voxel-wise, and can be computed as

$$\mathrm{SNR}(\boldsymbol{n}) = |\theta_1(\boldsymbol{n})|/\sigma_\eta, \quad [7]$$

where $\boldsymbol{n}$ is the spatial position. The SNR=30 was the lowest SNR obtained in knee cartilage measurements, and SNR=125 was the mean value. The SNR values were fixed in the synthetic experiments.

### 2.5. Optimizing Spin-Lock Times using Cramér-Rao Lower Bounds:

The CRLB asserts a lower bound on the variance of any unbiased estimator (15). In multi-parameter estimators, the Cramér-Rao matrix (CRM), defined as $\boldsymbol{V}(\boldsymbol{t}, \boldsymbol{\theta})$, is given by:

$$\boldsymbol{V}(\boldsymbol{t}, \boldsymbol{\theta}) = \boldsymbol{I}^{-1}(\boldsymbol{t}, \boldsymbol{\theta}), \quad [8]$$

where $\boldsymbol{I}(\boldsymbol{t}, \boldsymbol{\theta})$ is the Fisher information matrix (FIM), given by:

$$\boldsymbol{I}(\boldsymbol{t}, \boldsymbol{\theta}) = \mathbb{E}\left[\left(\frac{\partial ln\rho(\boldsymbol{x}(\boldsymbol{t}, \boldsymbol{\theta}))}{\partial \boldsymbol{\theta}}\right)\left(\frac{\partial ln\rho(\boldsymbol{x}(\boldsymbol{t}, \boldsymbol{\theta}))}{\partial \boldsymbol{\theta}}\right)^T \middle| \boldsymbol{t}, \boldsymbol{\theta}\right]. \quad [9]$$

where $\boldsymbol{x}(\boldsymbol{t}, \boldsymbol{\theta}) = [x(t_1, \boldsymbol{\theta}), \ldots, x(t_K, \boldsymbol{\theta})]^T$ and $\rho(\boldsymbol{x}(\boldsymbol{t}, \boldsymbol{\theta}))$ ln is the natural logarithm of the probability density function of the signal given by Equation 2 or 3. Explicit forms of the FIM for the models in Equations 2 and 3 are in the Appendix. The $i$-th diagonal element of the CRM in Equation 8 represents the lower bound of the variance of the estimated $i$-th parameter, written as:

$$\mathrm{Var}(\hat{\theta}_i) \ge [\boldsymbol{V}(\boldsymbol{t}, \boldsymbol{\theta})]_{i,i} \quad [10]$$

The CRM depends on the TSLs $\boldsymbol{t}$ used in the acquisition and the model parameters $\boldsymbol{\theta}$. The parameters depend on the expected values according to the anatomy, such as knee cartilage. We used in the optimization the values obtained with the procedure from section 2.4.

We are interested in $\boldsymbol{t}$ that minimizes the CRLB averaged over the parameters $\boldsymbol{\theta}$ expected in the cartilage. The optimization of the weighted averaged CRLB is stated as:

$$\hat{\boldsymbol{t}} = \arg\min_{\boldsymbol{t}\in\boldsymbol{T}} \frac{1}{S}\sum_{s=1}^{S}\left(\sum_i \omega_i [\boldsymbol{V}(\boldsymbol{t},\boldsymbol{\theta}_s)]_{i,i}\right), \quad [11]$$

where $\omega_i$ is the weight of a particular parameter, and it is used to weigh the importance of the parameters. In this work, we are just interested in improving the $T_{1\rho}$ value of the exponential model, given by $\theta_2$, regardless of $\theta_1$, using $\omega_1 = 0$ and $\omega_2 = 1$. The TSLs $\boldsymbol{t}$ should be in a pre-defined grid $\boldsymbol{T}$. In this study, $\boldsymbol{T}$ corresponds to a grid of possible TSLs between 1 and 55 ms, spaced by 1 ms. Where $\boldsymbol{\theta}_s$ is the $s$-th sample drawn from the distribution of the parameters of the anatomy or object.

We are particularly interested in the following *Modified CRLB* criterion that resembles the mean of the normalized absolute error (NAE), which leads to:

$$\hat{\boldsymbol{t}} = \arg\min_{\boldsymbol{t}\in\boldsymbol{T}} \frac{1}{S}\sum_{s=1}^{S}\left(\sum_i \omega_i \frac{\sqrt{|[\boldsymbol{V}(\boldsymbol{t},\boldsymbol{\theta}_s)]_{i,i}|}}{|[\boldsymbol{\theta}_s]_i|}\right). \quad [12]$$

This is the squared root of the magnitude of the element in the CRM weighted by the magnitude of the component, which favors equal relative precision across the components (11), and is more robust since it avoids that large $\boldsymbol{V}(\boldsymbol{t},\boldsymbol{\theta})$ dominates the overall cost (41). This is also connected to the mean of coefficient of variations (CV) over a set of possible parameters.

Because the optimization of the CRLB is an exact (i.e. non-noisy) optimization, any method for combinatorial problems can be used. We used recently-developed subset selection methods such as Pareto Optimization for Subset Selection (POSS) (42,43).

### 2.6. Matched Sampling-Fitting Optimization:

CRLB criteria are connected to the use of unbiased estimation methods for fitting (16,17) and optimize the lower bound for the variance of the estimated parameters (15). This does make the Hessian matrix (or its approximation using the Jacobian matrix) involved in NLS methods more stable, with a better condition number (19,44). However, this does not necessarily mean that the chosen $\boldsymbol{t}$ will provide the best performance on a particular fitting method. Note that iterative fitting methods for NLS, such as CGSTR (39) or Levenberg-Marquardt (18), are not necessarily unbiased estimators. They have their approaches to deal with the ill-conditioning of the non-linear system (18). This means that CRLB may not be a fundamental bound in this context. Besides, fitting methods based on ANNs may have no benefit by using CRLB-optimized TSLs.

Following the arguments of data-driven approaches for MRI that optimizes the k-space sampling according to the recovery method (20–22), where it was observed that a matched sampling-reconstruction is more effective, we decided to modify the TSLs optimization to include the fitting algorithm. CRLB is partially symbolic, using the model derivative and statistical expectation of the second-order moment of the noise, and partially numerical, using numerical values of $\boldsymbol{\theta}$. In contrast, sampling-fitting approaches are purely numerical, even though the data can be generated from analytical models, as we did in this work.

Considering $\boldsymbol{\theta}_s$ as the $s$-th sample of the expected parameters, and $\boldsymbol{x}_s$ is the noisy signal generated with $\boldsymbol{\theta}_s$ from Equation 2, the fitting algorithm returns the estimated $\widehat{\theta}_s = R(\boldsymbol{t}; \boldsymbol{x}_s)$, assuming that the TSL schedule $\boldsymbol{t}$ was used to generate $\boldsymbol{x}_s$. The proposed criterion considers the following minimization problem:

$$\widehat{\boldsymbol{t}} = \arg\min_{\boldsymbol{t} \in \boldsymbol{T}} F(\boldsymbol{t}), \quad [13]$$

being:

$$F(\boldsymbol{t}) = \frac{1}{S} \sum_{s=1}^{S} d(\boldsymbol{\theta}_s, R(\boldsymbol{t}; \boldsymbol{x}_s)), \quad [14]$$

where $d\left(\boldsymbol{\theta}, \widehat{\boldsymbol{\theta}}\right)$ is a measurement of the distance between the exact parameters $\boldsymbol{\theta}$ and its estimation $\widehat{\boldsymbol{\theta}}$. One possible choice for $d\left(\boldsymbol{\theta}, \widehat{\boldsymbol{\theta}}\right)$ is the weighted squared error, given by:

$$d\left(\boldsymbol{\theta}, \widehat{\boldsymbol{\theta}}\right) = \sum_{i=1}^{2} \omega_i \left|\theta_i - \widehat{\theta}_i\right|^2, \quad [15]$$

leading Equation 13 to the optimization of the mean squared error (MSE), where $\omega_i$ is the weight on the $i$-th element of $\boldsymbol{\theta}$, which we denominated MSF-MSE. Another possible cost function is to use the normalized absolute error (NAE) of each parameter, given by:

$$d\left(\boldsymbol{\theta}, \widehat{\boldsymbol{\theta}}\right) = \sum_{i=1}^{2} \omega_i \frac{\left|\theta_i - \widehat{\theta}_i\right|}{\left|\theta_i\right|}, \quad [16]$$

leading Equation 13 to the optimization of the mean of the normalized absolute error (MNAE), denominated MSF-MNAE, which is also related to the coefficient of variations.

The learning problem in Equation 13 uses samples of the signal $\boldsymbol{x}_s$, generated according to Equation 2, considering the current $\boldsymbol{t}$, $\eta$, and $\boldsymbol{\theta} = [\theta_1\ \theta_2]^T$. We used values obtained with the procedure described in section 2.4.

Note that the cost function in Equation 13 is noisy (33), because the cost $d(\boldsymbol{\theta}_s, R(\boldsymbol{t}, \boldsymbol{x}_s))$ requires to compute $R(\boldsymbol{t}; \boldsymbol{x}_s)$, where the signal $\boldsymbol{x}_s$ is generated with random noise. This makes the optimization problem also noisy, and the optimization algorithm must be aware of it.

Algorithm 1 is a modification of Pareto Optimization for Noisy Subset Selection (PONSS) (33,42), denoted here as Modified PONSS. Similar to PONSS, a group of candidate solutions is stored in the set $\boldsymbol{C}$. At each iteration of Algorithm 1, one element of $\boldsymbol{C}$, defined as $\boldsymbol{t}$, is selected (in line 5) and modified (in line 6) by changing one of its elements in the composition of a new candidate as $\boldsymbol{t}'$. The modification is a random switch of one of its time points to a new point in a pre-defined grid $\boldsymbol{T}$. The new candidate $\boldsymbol{t}'$ will be accepted in the set $\boldsymbol{C}$ if $F(\boldsymbol{t}') < F(\boldsymbol{t}_{best}) + 2b$.

Because $F(\boldsymbol{t})$ is noisy, one needs to include the dispersion of the values of the cost function, represented by $b$. In the same way as PONSS, good candidates in the $\pm b$ range are not discarded. However, since the size of the set $\boldsymbol{C}$ may grow significantly, a new evaluation of the cost function is done between lines 12 and 15 of Algorithm 1, also called a tie-break

in (33). In the regular PONSS, in (33), a new sample of $F(\boldsymbol{t})$ is drawn from each $\boldsymbol{t} \in \boldsymbol{C}$, while previous $F(\boldsymbol{t})$'s are forgotten. Here, in the Modified PONSS, the new samples are proportionally averaged to the mean $F(\boldsymbol{t})$, (in line 14), leading the optimization to the mean value of the noisy cost function. As more tie-breaks are done, more samples of $F(\boldsymbol{t})$ are drawn, producing better estimations of the mean $F(\boldsymbol{t})$'s.

**Algorithm 1**: Modified PONSS

1. $\boldsymbol{C} \leftarrow \{\boldsymbol{t}_{init}\}$
2. $\boldsymbol{t}_{best} \leftarrow \boldsymbol{t}_{init}$
3. $l \leftarrow 1$
4. **While** $l \leq L$ **do**
5. $\quad \boldsymbol{t} \leftarrow$ **select** $\boldsymbol{t}$ **from** $\boldsymbol{C}$ **uniformly at random**
6. $\quad \boldsymbol{t}' \leftarrow$ **modify − one − element**$(\boldsymbol{t}, \boldsymbol{T})$
7. $\quad F(\boldsymbol{t}') \leftarrow$ **draw a sample of** $F(\boldsymbol{t}')$
8. $\quad$ **if** $F(\boldsymbol{t}') < F(\boldsymbol{t}_{best})$
9. $\quad\quad \boldsymbol{t}_{best} \leftarrow \boldsymbol{t}'$
10. $\quad$ **if** $F(\boldsymbol{t}') < F(\boldsymbol{t}_{best}) + 2b$
11. $\quad\quad \boldsymbol{C} \leftarrow \boldsymbol{C} \backslash \{\boldsymbol{t} \in \boldsymbol{C} | F(\boldsymbol{t}) \geq F(\boldsymbol{t}_{best}) + 2b\} \cup \{\boldsymbol{t}'\}$
12. $\quad$ **if** $|\boldsymbol{C}| = \mathrm{B} + 1$ (perform tie break)
13. $\quad$ **For** $\{\boldsymbol{t} \in \boldsymbol{C}\}$
14. $\quad\quad$ **draw a new sample of** $F(\boldsymbol{t})$ **and proportionally averages with old** $F(\boldsymbol{t})$
15. $\quad$ **keep the best** B **elements of** $\boldsymbol{C}$**, selecting the new** $\boldsymbol{t}_{best}$
16. $\quad l \leftarrow l + 1$
17. **Return** $\boldsymbol{t}_{best}, \boldsymbol{C}$

### 2.7. Analysis of Estimated $T_{1\rho}$ Values:

To validate the results, we compare the estimated $T_{1\rho}$ values obtained with different TSLs against reference values. In the synthetic experiments, the exact $T_{1\rho}$ values are known. For the other cases, the reference values are estimated using all TSLs acquired in each scanning session. We used the MNAE:

$$MNAE = \frac{1}{|ROI|} \sum_{\boldsymbol{n} \in ROI} \frac{\left|\theta_2(\boldsymbol{n}) - \hat{\theta}_2(\boldsymbol{n})\right|}{|\theta_2(\boldsymbol{n})|}, \quad [17]$$

and normalized root MSE (NRMSE):

$$NRMSE = \sqrt{\frac{\sum_{\boldsymbol{n} \in ROI} \left|\theta_2(\boldsymbol{n}) - \hat{\theta}_2(\boldsymbol{n})\right|^2}{\sum_{\boldsymbol{n} \in ROI} |\theta_2(\boldsymbol{n})|^2}}. \quad [18]$$

The sums consider the voxels $\boldsymbol{n}$ in the region of interest (ROI), where $|ROI|$ is the number of voxels in the ROI. The ROI was manually segmented. Also, $\theta_2(\boldsymbol{n})$ is the reference value of a particular voxel, and $\hat{\theta}_2(\boldsymbol{n})$ is its estimation using the TSL schedule being evaluated.

To assess repeatability, we evaluate the coefficient of variations (CV), which corresponds to RMS CV used in (45). For agar gel phantoms the sessions were repeated one after the other without moving the phantom. We also assessed linear predictability between agar gel concentrations and $R_{1\rho}$ values by using the coefficient of determination ($R^2$). For healthy volunteer scans, motion correction was used to register the knees in the same position.

## 3. RESULTS

### 3.1. Illustration of Noisy Cost Functions and Stability of the Modified CRLB:

In Figure 2 we illustrate the issue with noisy cost functions and the stability of the modified CRLB using curves related to small problems (K=2). Figure 2(a) shows CRLB and Modified CRLB for optimizing TSLs targeting the models in Equations 2 and 3. If the objective is improving $T_{1\rho}$, then the FIM, shown in Equation A1 in theAppendix, has its components as in Equation A2. On the other hand, if the objective is improving $R_{1\rho}$, then the components of FIM should be as in Equation A3. Note that when the $T_{1\rho}$ value is estimated, the $R_{1\rho}$ value is automatically obtained. However, from the point of view of the CRLB optimization, they are different things and have different optimal TSLs. In this sense, the Modified CRLB has the advantage of being invariant to this choice, as seen in Figure 2(a). No matter if one is interested in improving $T_{1\rho}$ or $R_{1\rho}$ estimation, the optimal TSL sampling schedule is the same. Figure 2(b) shows a comparison of the two (non-noisy) CRLB criteria for $T_{1\rho}$ values (CRLB and the Modified CRLB) and the mean cost function (averaged from 15 realizations) of the two (noisy) MSF criteria (MSF-MSE and MSF-MNAE). Note that the optimal solutions for the Modified CLRB and MSF-MNAE are much closer to one another than the CRLB and MSF-MSE. Figures 2(a) and 2(b) illustrate the stability of the Modified CRLB.

Because the MSF cost functions are noisy, each realization may have a different minimum. In Figure 2(c), it is shown the curves for two different realizations. Optimization methods for exact cost functions are likely to converge to the optimum of one realization because they expect the evaluations of $F(\boldsymbol{t})$ to be exact. Since they are not exact, we need a method able to converge to the optimal solution of the mean cost function. To achieve this, the optimization method needs to average among multiple measures of $F(\boldsymbol{t})$. Also, the value of $b$ in Modified PONSS should be chosen considering the dispersion of the noisy cost function around its mean value. This can be seen in Figures 2(d), which shows the mean cost function and a range of values (±3 st.dev.) where 99.73% of the realizations are expected to be.

### 3.2. Evaluation of the Optimized TSLs for Synthetic Data:

The evaluation of the methods with synthetic data is composed of 15 repetitions of the sampling-fitting, using S=5000 samples of exponential functions generated according to the model from Equation 2, with parameters ($\theta_1$ and $\theta_2$) obtained as described in section 2.4.

The non-optimized and optimized TSLs, for different K, are shown in Table 1 for SNR=30 and in Supporting Information Table S1 (in the supplemental information) for SNR=125 showing the MNAE and NRMSE, in percentages. Note that optimized TSLs with K=2 are approximately equal in quality to non-optimized with K=3, and optimized TSLs with K=3

are equivalent to non-optimized with K=4. In Figure 3, we see the performance of some TSL schedules for individualized $T_{1\rho}$ values in the range used in this experiment. This figure shows an average of 500 repetitions for each $T_{1\rho}$ value. The resulting curve (with lower MNAE) shows the reduced estimation error for $T_{1\rho}$ values (with low MNAE) in the expected range. Note that the estimation error is different for each $T_{1\rho}$ and each TSL schedule favors some $T_{1\rho}$ values.

### 3.3. Experiments with $T_{1\rho}$ Model Phantoms:

The reference $T_{1\rho}$ map of the model phantom (composed of tubes with 2%, 3%, 4%, 5%, and 6% agar gel) is shown in Figure 5(a). It was computed using all the 16 TSLs acquired in the session (1, 1, 3, 10, 20, 25, 30, 32, 32, 34, 34, 38, 40, 40, 42, 55 ms). Figures 4 shows the linear regression between agar gel concentrations and $R_{1\rho}$ values. The strong coefficient of determination ($R^2$) with $R_{1\rho}$ values shows the linear predictability between agar gel concentrations and $R_{1\rho}$ values. One-dimensional histograms of the $T_{1\rho}$ values for the first and second scans of the phantom are shown in Figure 5(b). Some illustrative examples of $T_{1\rho}$ maps and their voxel-wise error related to the reference are shown in Figure 5(c)–(f). These examples illustrate the improvement in the maps and reduction of error with optimization of the TSLs. Table 2 shows all the results with model phantoms computed from 10 slices of the $T_{1\rho}$ phantom.

### 3.4. Experiments with In Vivo Knee Cartilage Data:

In-vivo knee cartilage data from five volunteers were acquired. A non-optimized scan of one of the volunteers was used to obtain parameters for training, as described in section 2.4. In Figure 7(e) a 2D histogram showing the pair of $T_{1\rho}$ and SNR (as defined in Equation 7) values of the volunteer used for training is presented. The 2D histogram of one of the other volunteers is shown in Figure 7(m), with its respective 1D versions for each repeated scan in Figures 6(e) and 6(m).

In each scanning session, a total of 15 TSLs were acquired to compose all optimized and non-optimized TSLs needed for the comparison (only K =2 and K =3 were compared to avoid long scanning sessions). The reference $T_{1\rho}$ map was computed using the values measured from all the 15 TSLs (TSLs=1, 1, 3, 10, 20, 25, 30, 31, 32, 36, 37, 40, 42, 47, 55 ms). One of the volunteers was scanned twice, one week apart, for repeatability evaluation. The MNAE, NRMSE, and CV are shown in Table 3. Figure 6 shows some illustrative $T_{1\rho}$ maps and voxel-wise errors (related to the reference) to compare optimized and non-optimized TSLs for medial cartilage. Also, the first and second scans of one volunteer are shown (same slice) to illustrate the repeatability. Figure 7 shows similar results for the lateral cartilage.

## 4. DISCUSSION

### 4.1. Fitting with Non-Linear Least Squares and Artificial Neural Networks:

The $T_{1\rho}$ mapping results using NLS or ANN are very similar in terms of quality, as seen in Tables 1, 2, 3, and Supporting Information Table S1, more than previously reported (23). ANNs are computationally advantageous when a large number of voxels are to be fitted.

Even though the training process takes some time (0.2~1 hours), the fitting process of new data is fast (2~10 sec).

While the difference in quality according to the fitting method is not large in this problem, the difference in quality according to the chosen TSL is. Using optimal TSLs improved both fitting approaches, NLS and ANN, by larger margins, especially for small K, as seen in the tables.

### 4.2. Difficulties of the Optimization of MSF and Advantages of CRLB:

Algorithms like POSS can find the optimal solution for CRLB criteria relatively quickly, taking from 10 minutes to 1 hour in our problems, because the cost function only needs to be evaluated once for a particular $\boldsymbol{t}$. On the other hand, optimizing any of the MSF criteria is more difficult. Cost functions are more expensive to evaluate since it requires to perform the fitting process, and they have to be evaluated multiple times for improved precision. The finer the precision of the grid $\boldsymbol{T}$, the more evaluations are needed to properly resolve which $\boldsymbol{t}$ is optimal. Because of these issues, algorithms like the Modified PONSS require a longer optimization time, in the order of 10 to 100 times more cost function evaluations than with exact cost functions (from 1 day to a couple of weeks in our problems). This long optimization time is not always worthwhile, considering that CRLB criteria, which is easier to optimize, obtain very close quality results.

### 4.3. Robustness of the Modified CRLB and MSF-MNAE:

As seen in Figure 2(a), the CRLB is sensitive to the exponential model used, leading to different optimal TSLs for $T_{1\rho}$ and $R_{1\rho}$. In contrast, the Modified CRLB was insensitive to choice for $T_{1\rho}$ or $R_{1\rho}$. The MSF-MNAE also shares the same robustness property, as seen in Figure 2(b), producing stable results across the different experiments than the ordinary CRLB and MSF-MSE.

### 4.4. Stability and Unicity of the Optimal TSLs:

Note that the optimization of the TSLs is a non-convex problem. In this sense, there is no guarantee of uniqueness. On top of it, the optimal TSLs are usually in a plateau in the cost function (a plateau is a region of the cost function where the cost is approximately equal), as seen in Figure 2, particularly in Figure 2(a) and 2(b). This explains why different TSL schedules performed almost equally well in most experiments, particularly with large K. In this sense, the resulting TSLs provided in Tables 1, 2, and 3 and Supporting Information Table S1 should not be taken as the unique optimal TSL because other non-tested TSLs schedules may perform equally well. Note also that, as shown in Figure 3, that a particular choice of TSL schedule may perform better for some $T_{1\rho}$ values than the others. This usually depends on the given distribution $T_{1\rho}$ values of and the chosen criterion.

### 4.5. Comparison with Previous Studies:

In (7) only linear fitting in the magnitude values was considered. Here we rely on the fact that complex-valued fitting, being it done by NLS or ANNs, is more precise, and we also assessed different optimization criteria. Even though the precision of the grid $\boldsymbol{T}$ in (7) is small (TSLs spaced by 10 ms), some similarities among optimal values are observed: the

first TSL is usually in the smallest position of the grid while the others are clustered nearby in mid to large positions. Similar results have already been shown in (46). In some sense, the optimal TSLs we obtained contradicted our previous intuition that good TSLs should be spread in time (34,47). Plots like in Figure 3 can help to check if certain expected $T_{1\rho}$ values are well-covered by the chosen TSL schedule.

In (8,9) the worst-case of the CRLB for the expected range of parameters was optimized, instead of the mean-case considered in Equations 11. Worst-case optimization focus on reducing the cost for the worst parameter in the range of expected parameter values. The mean of the CRLB, on the other hand, depends on the expected distribution of parameters, giving more importance to more frequent parameters. Mean-case is more accurate when the distribution is known and stable across different scanned subjects.

In (11) worst-case of the Modified CRLB for the expected range of parameters was optimized. This is the same modification of the CRLB parameters done in Equation 12, except that in Equation 12 the mean is optimized. In (13), the mean-case optimization with a cost function similar to Equations 11 was used for MR fingerprinting. To the best of our knowledge, no other study compared different CRLB approaches and different MSF approaches with various fitting methods to find which one is better for choosing the TSL sampling schedules.

### 4.6. Limitations of This Study and Future Directions

In this study, we considered Gaussian noise in complex-valued fitting algorithms, assuming the image reconstruction returns a complex-valued image. Magnitude-only fitting, outliers, and problems with motion other than translation motion are not considered here. For the magnitude-only fitting, Rician noise is more adequate than Gaussian noise (48). Under outliers and complex motion, approaches based on robust statistics (46) can perform better. Also, ANN can be trained with these problems, possibly overcoming them in a more simplified and advantageous computational manner than robust fitting methods.

The approaches discussing here can also be applied to other quantitative mapping techniques, such as $T_1$ and $T_2$ mapping (8–12,16), and diffusion measurements (49). Also, these approaches can be extended with sophisticated multi-compartment models such as biexponential (34,50), stretched exponential (51,52) models.

We did not discuss k-space undersampling as a way to reduce scan time for $T_{1\rho}$ mapping in this study, only the scan time reduction by reducing the number of TSLs. In this sense, we observe that the TSLs optimized by the Modified CRLB and MSF-MNAD performed well even when 2 TSLs were used. Nevertheless, k-space undersampling, specially optimized k-space undersampling (22), can be combined with optimized TSL for even faster and stable $T_{1\rho}$ mapping.

## 5. CONCLUSION

In this work, different optimization criteria for choosing the spin-lock times in $T_{1\rho}$ mapping were compared. According to our results in synthetic data, model phantoms,

and healthy volunteers, a modified CRLB and the MSF based on MNAE were the most robust optimization approaches for choosing TSLs. The Modified CRLB was easier to optimize since this criterion has exact (non-noisy) cost functions. The optimized TSLs with these methods allowed robust results with improved quality when using only 2 TSLs and complex-valued fitting with iterative NLS or ANN.

## Supplementary Material

Refer to Web version on PubMed Central for supplementary material.

## Acknowledgment

This study was supported by NIH grants, R21-AR075259-01A1, R01-AR068966, R01-AR076328-01A1, R01-AR076985-01A1, and R01-AR078308-01A1 and was performed under the rubric of the Center of Advanced Imaging Innovation and Research (CAI2R), an NIBIB Biomedical Technology Resource Center (NIH P41-EB017183).

## APPENDIX

## Fisher Information Matrix used in CRLB optimization:

The FIM for CRLB optimization with the $T_{1\rho}$ model from Equation 2 can be written as

$$\boldsymbol{I}(\boldsymbol{t},\boldsymbol{\theta}) = \frac{1}{\sigma_\eta^2}\sum_{k=1}^{K} \boldsymbol{J}(t_k,\boldsymbol{\theta})^H \boldsymbol{J}(t_k,\boldsymbol{\theta}), \quad [A1]$$

with

$$\boldsymbol{J}(t_k,\boldsymbol{\theta}) = \left[exp(-t_k/\theta_2) \quad \left(t_k\theta_1/\theta_2^2\right)exp(-t_k/\theta_2)\right], \quad [A2]$$

where $J(t_k, \boldsymbol{\theta})^H$ is the transpose and complex-conjugate version of $J(t_k, \boldsymbol{\theta})$. Note that the $R_{1\rho}$ model from Equation 3 can also be used. In this case

$$\boldsymbol{J}(t_k,\boldsymbol{\theta}) = \left[exp\left(-\bar{\theta}_2 t_k\right) \quad -(t_k\theta_1)exp\left(-\bar{\theta}_2 t_k\right)\right]. \quad [A3]$$

## REFERENCES

1. Akella SVS, Reddy Regatte R, Gougoutas AJ, et al. Proteoglycan-induced changes in T1ρ-relaxation of articular cartilage at 4T. Magn. Reson. Med 2001;46:419–423 doi: 10.1002/mrm.1208. [PubMed: 11550230]
2. Nishioka H, Nakamura E, Hirose J, Okamoto N, Yamabe S, Mizuta H. MRI T1ρ and T2 mapping for the assessment of articular cartilage changes in patients with medial knee osteoarthritis after hemicallotasis osteotomy. Bone Jt. Res 2016;5:294–300 doi: 10.1302/2046-3758.57.BJR-2016-0057.R1.
3. MacKay JW, Low SBL, Smith TO, Toms AP, McCaskie AW, Gilbert FJ. Systematic review and meta-analysis of the reliability and discriminative validity of cartilage compositional MRI in knee osteoarthritis. Osteoarthr. Cartil 2018;26:1140–1152 doi: 10.1016/j.joca.2017.11.018.
4. Redpath TW. Signal-to-noise ratio in MRI. Br. J. Radiol 1998;71:704–707 doi: 10.1259/bjr.71.847.9771379. [PubMed: 9771379]
5. Bernstein M, King K, Zhou X. Handbook of MRI pulse sequences. Academic Press; 2004.

6. Ohliger MA, Sodickson DK. An introduction to coil array design for parallel MRI. NMR Biomed. 2006;19:300–315 doi: 10.1002/nbm.1046. [PubMed: 16705631]
7. Johnson CP, Thedens DR, Magnotta VA. Precision-guided sampling schedules for efficient T1ρ mapping. J. Magn. Reson. Imaging 2015;41:242–250 doi: 10.1002/jmri.24518. [PubMed: 24474423]
8. Funai A, Fessler JA. Cramér Rao bound analysis of joint B1/T1 mapping methods in MRI. In: IEEE International Symposium on Biomedical Imaging. IEEE International Symposium on Biomedical Imaging IEEE; 2010. pp. 712–715. doi: 10.1109/ISBI.2010.5490075.
9. Nataraj G, Nielsen J-F, Fessler JA. Optimizing MR Scan Design for Model-Based T1, T2 Estimation From Steady-State Sequences. IEEE Trans. Med. Imaging 2017;36:467–477 doi: 10.1109/TMI.2016.2614967. [PubMed: 27893386]
10. Hernando D, Kramer JH, Reeder SB. Multipeak fat-corrected complex R2* relaxometry: Theory, optimization, and clinical validation. Magn. Reson. Med 2013;70:1319–1331 doi: 10.1002/mrm.24593. [PubMed: 23359327]
11. Teixeira RPAG, Malik SJ, Hajnal JV. Joint system relaxometry (JSR) and Crámer-Rao lower bound optimization of sequence parameters: A framework for enhanced precision of DESPOT T 1 and T 2 estimation. Magn. Reson. Med 2018;79:234–245 doi: 10.1002/mrm.26670. [PubMed: 28303617]
12. Shrager RI, Weiss GH, Spencer RGS. Optimal time spacings for T2 measurements: monoexponential and biexponential systems. NMR Biomed. 1998;11:297–305 doi: 10.1002/(SICI)1099-1492(199810)11:6<297::AID-NBM531>3.0.CO;2-A. [PubMed: 9802472]
13. Zhao B, Haldar JP, Liao C, et al. Optimal Experiment Design for Magnetic Resonance Fingerprinting: Cramér-Rao Bound Meets Spin Dynamics. IEEE Trans. Med. Imaging 2019;38:844–861 doi: 10.1109/TMI.2018.2873704. [PubMed: 30295618]
14. Assländer J A Perspective on MR Fingerprinting. J. Magn. Reson. Imaging 2021;53:676–685 doi: 10.1002/jmri.27134. [PubMed: 32286717]
15. Kay SM. Fundamentals of Statistical Signal Processing, Volume I: Estimation Theory. Prentice Hall; 1993.
16. Lewis CM, Hurley SA, Meyerand ME, Koay CG. Data-driven optimized flip angle selection for T1 estimation from spoiled gradient echo acquisitions. Magn. Reson. Med 2016;76:792–802 doi: 10.1002/mrm.25920. [PubMed: 26361720]
17. Basu S, Bresler Y. The stability of nonlinear least squares problems and the Cramer-Rao bound. IEEE Trans. Signal Process 2000;48:3426–3436 doi: 10.1109/78.887032.
18. Madsen K, Nielsen HB, Tingleff O. Methods for Non-Linear Least Squares Problems. 2nd ed. Technical University of Denmark, DTU; 2004.
19. Kirsch A Regularization by Discretization. In: An Introduction to the Mathematical Theory of Inverse Problems. An Introduction to the Mathematical Theory of Inverse Problems.; 2011. pp. 63–119. doi: 10.1007/978-1-4419-8474-6_3.
20. Gözcü B, Sanchez T, Cevher V. Rethinking Sampling in Parallel MRI: A Data-Driven Approach. In: European Signal Processing Conference. European Signal Processing Conference IEEE; 2019. pp. 1–5. doi: 10.23919/EUSIPCO.2019.8903150.
21. Gözcü B, Mahabadi RK, Li YH, et al. Learning-based compressive MRI. IEEE Trans. Med. Imaging 2018;37:1394–1406 doi: 10.1109/TMI.2018.2832540. [PubMed: 29870368]
22. Zibetti MVW, Herman GT, Regatte RR. Fast data-driven learning of parallel MRI sampling patterns for large scale problems. Sci. Rep 2021;11:19312 doi: 10.1038/s41598-021-97995-w. [PubMed: 34588478]
23. Bishop CM, Roach CM. Fast curve fitting using neural networks. Rev. Sci. Instrum 1992;63:4450–4456 doi: 10.1063/1.1143696.
24. Jung S, Lee H, Ryu K, et al. Artificial neural network for multi-echo gradient echo–based myelin water fraction estimation. Magn. Reson. Med 2021;85:380–389 doi: 10.1002/mrm.28407. [PubMed: 32686208]
25. Bertleff M, Domsch S, Weingärtner S, et al. Diffusion parameter mapping with the combined intravoxel incoherent motion and kurtosis model using artificial neural networks at 3 T. NMR Biomed. 2017;30:e3833 doi: 10.1002/nbm.3833.

26. Domsch S, Mürle B, Weingärtner S, Zapp J, Wenz F, Schad LR. Oxygen extraction fraction mapping at 3 Tesla using an artificial neural network: A feasibility study. Magn. Reson. Med 2018;79:890–899 doi: 10.1002/mrm.26749. [PubMed: 28504360]
27. Balasubramanyam C, Ajay MS, Spandana KR, Shetty AB, Seetharamu KN. Curve fitting for coarse data using artificial neural network. WSEAS Trans. Math 2014;13:406–415.
28. Liu F, Feng L, Kijowski R. MANTIS: Model-Augmented Neural neTwork with Incoherent k-space Sampling for efficient MR parameter mapping. Magn. Reson. Med 2019;82:174–188 doi: 10.1002/mrm.27707. [PubMed: 30860285]
29. Hammernik K, Klatzer T, Kobler E, et al. Learning a variational network for reconstruction of accelerated MRI data. Magn. Reson. Med 2018;79:3055–3071 doi: 10.1002/mrm.26977. [PubMed: 29115689]
30. Knoll F, Hammernik K, Zhang C, et al. Deep-learning methods for parallel magnetic resonance imaging reconstruction: A survey of the current approaches, trends, and issues. IEEE Signal Process. Mag 2020;37:128–140 doi: 10.1109/MSP.2019.2950640. [PubMed: 33758487]
31. Liu F, Kijowski R, El Fakhri G, Feng L. Magnetic resonance parameter mapping using model-guided self-supervised deep learning. Magn. Reson. Med 2021;85:3211–3226 doi: 10.1002/mrm.28659. [PubMed: 33464652]
32. Feng L, Ma D, Liu F. Rapid MR relaxometry using deep learning: An overview of current techniques and emerging trends. NMR Biomed. 2020:e4416 doi: 10.1002/nbm.4416. [PubMed: 33063400]
33. Qian C, Shi JC, Yu Y, Tang K, Zhou ZH. Subset selection under noise. In: Advances in Neural Information Processing Systems. Vol. 2017-Decem. Advances in Neural Information Processing Systems.; 2017. pp. 3561–3571.
34. Sharafi A, Xia D, Chang G, Regatte RR. Biexponential T 1ρ relaxation mapping of human knee cartilage in vivo at 3 T. NMR Biomed. 2017;30:e3760 doi: 10.1002/nbm.3760.
35. Pruessmann KP, Weiger M, Scheidegger MB, Boesiger P. SENSE: Sensitivity encoding for fast MRI. Magn. Reson. Med 1999;42:952–962 doi: 10.1002/(SICI)1522-2594(199911)42:5<952::AID-MRM16>3.0.CO;2-S. [PubMed: 10542355]
36. Lustig M, Donoho DL, Pauly JM. Sparse MRI: The application of compressed sensing for rapid MR imaging. Magn. Reson. Med 2007;58:1182–1195 doi: 10.1002/mrm.21391. [PubMed: 17969013]
37. Zibetti MVW, De Pierro AR. Improving compressive sensing in MRI with separate magnitude and phase priors. Multidimens. Syst. Signal Process 2017;28:1109–1131 doi: 10.1007/s11045-016-0383-6.
38. Hernando D, Levin YS, Sirlin CB, Reeder SB. Quantification of liver iron with MRI: State of the art and remaining challenges. J. Magn. Reson. Imaging 2014;40:1003–1021 doi: 10.1002/jmri.24584. [PubMed: 24585403]
39. Steihaug T The conjugate gradient method and trust regions in large scale optimization. SIAM J. Numer. Anal 1983;20:626–637 doi: 10.1137/0720042.
40. Veraart J, Novikov DS, Christiaens D, Ades-aron B, Sijbers J, Fieremans E. Denoising of diffusion MRI using random matrix theory. Neuroimage 2016;142:394–406 doi: 10.1016/j.neuroimage.2016.08.016. [PubMed: 27523449]
41. Huber P, Ronchetti E. Robust statistics. 1981.
42. Qian C, Yu Y, Zhou ZH. Subset selection by Pareto optimization. In: Advances in Neural Information Processing Systems. Vol. 2015-Janua. Advances in Neural Information Processing Systems.; 2015. pp. 1774–1782.
43. Zhou Z-H, Yu Y, Qian C. Evolutionary learning: Advances in theories and algorithms. Singapore: Springer Singapore; 2019. doi: 10.1007/978-981-13-5956-9.
44. Hansen PC. Rank-Deficient and Discrete Ill-Posed Problems. Philadelphia, PA: Society for Industrial and Applied Mathematics; 1998. doi: 10.1137/1.9780898719697.
45. Mosher TJ, Zhang Z, Reddy R, et al. Knee articular cartilage damage in osteoarthritis: Analysis of MR image biomarker reproducibility in ACRIN-PA 4001 multicenter trial. Radiology 2011;258:832–842 doi: 10.1148/radiol.10101174. [PubMed: 21212364]

46. Zibetti MVW, Sharafi A, Regatte R. Robust Statistics for T1ρ-Mapping of Knee Cartilage on Mono- and Bi-Exponential Models : Optimal Spin-Lock Times and Fitting Methods. In: Proc. Intl. Soc. Mag. Res. Med. Proc. Intl. Soc. Mag. Res. Med; 2020.
47. Zibetti MVW, Sharafi A, Otazo R, Regatte RR. Accelerated mono- and biexponential 3D-T1ρ relaxation mapping of knee cartilage using golden angle radial acquisitions and compressed sensing. Magn. Reson. Med 2020;83:1291–1309 doi: 10.1002/mrm.28019. [PubMed: 31626381]
48. Bouhrara M, Spencer RG. Fisher information and Cramér-Rao lower bound for experimental design in parallel imaging. Magn. Reson. Med 2018;79:3249–3255 doi: 10.1002/mrm.26984. [PubMed: 29090485]
49. Brihuega-Moreno O, Heese FP, Hall LD. Optimization of diffusion measurements using Cramer-Rao lower bound theory and its application to articular cartilage. Magn. Reson. Med 2003;50:1069–1076 doi: 10.1002/mrm.10628. [PubMed: 14587018]
50. Sharafi A, Chang G, Regatte RR. Biexponential T2 relaxation estimation of human knee cartilage in vivo at 3T. J. Magn. Reson. Imaging 2018;47:809–819 doi: 10.1002/jmri.25778. [PubMed: 28561955]
51. Reiter DA, Magin RL, Li W, Trujillo JJ, Pilar Velasco M, Spencer RG. Anomalous T2 relaxation in normal and degraded cartilage. Magn. Reson. Med 2016;76:953–962 doi: 10.1002/mrm.25913. [PubMed: 26336966]
52. Johnston DC. Stretched exponential relaxation arising from a continuous sum of exponential decays. Phys. Rev. B 2006;74:184430 doi: 10.1103/PhysRevB.74.184430.

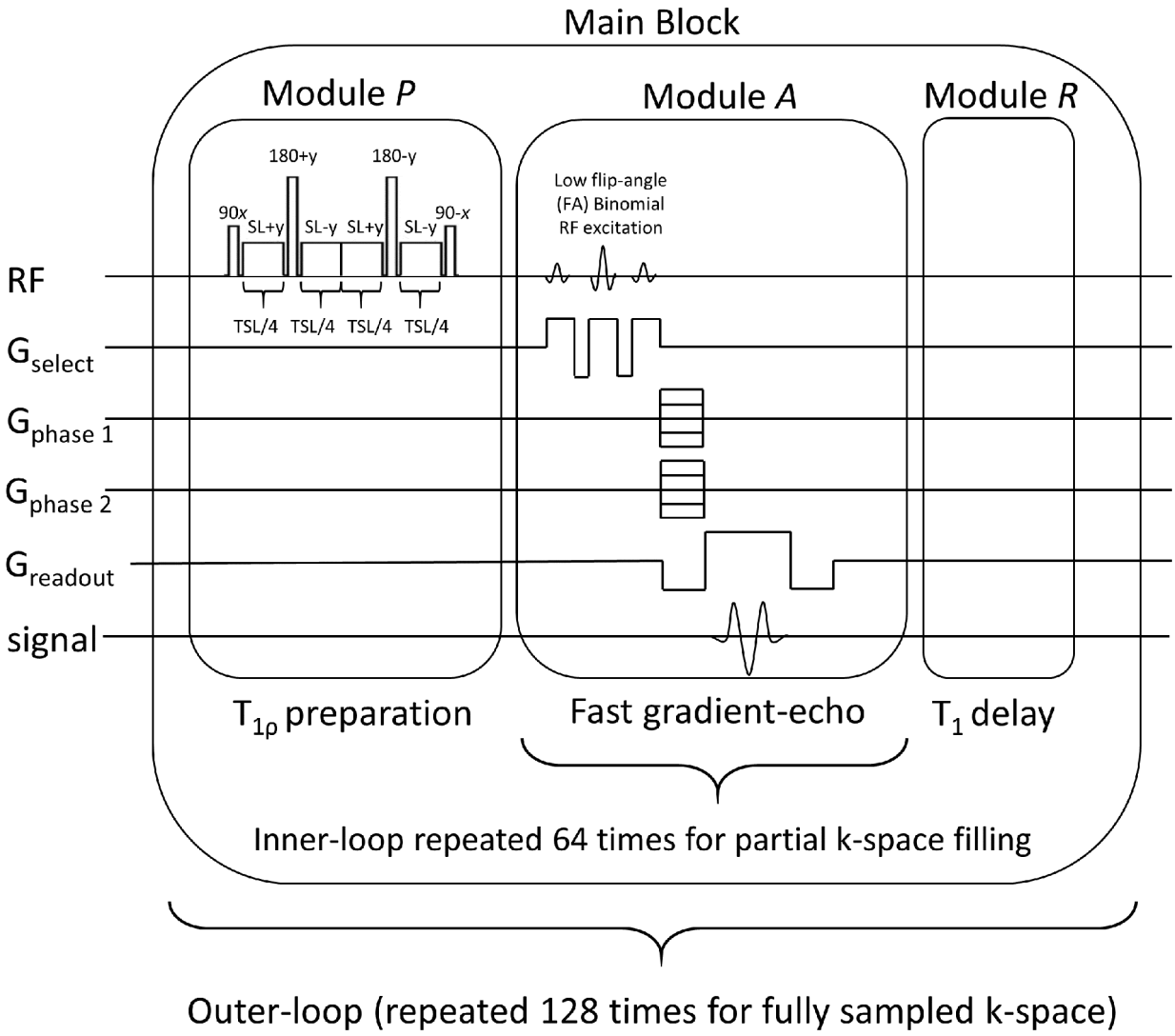


**Figure 1:**

Pulse sequence used to capture one $T_{1\rho}$-weighted 3D volume (one TSL). The pulse sequence is composed of a $T_{1\rho}$ preparation module *P*, that applies the $T_{1\rho}$ weighting, a 3D imaging module *A*, that acquires 64 k-space lines of the entire 3D k-space, and the longitudinal magnetization restoration module *R*, which recovers the main magnetization before the sequence be repeated until all 3D k-space lines are acquired.

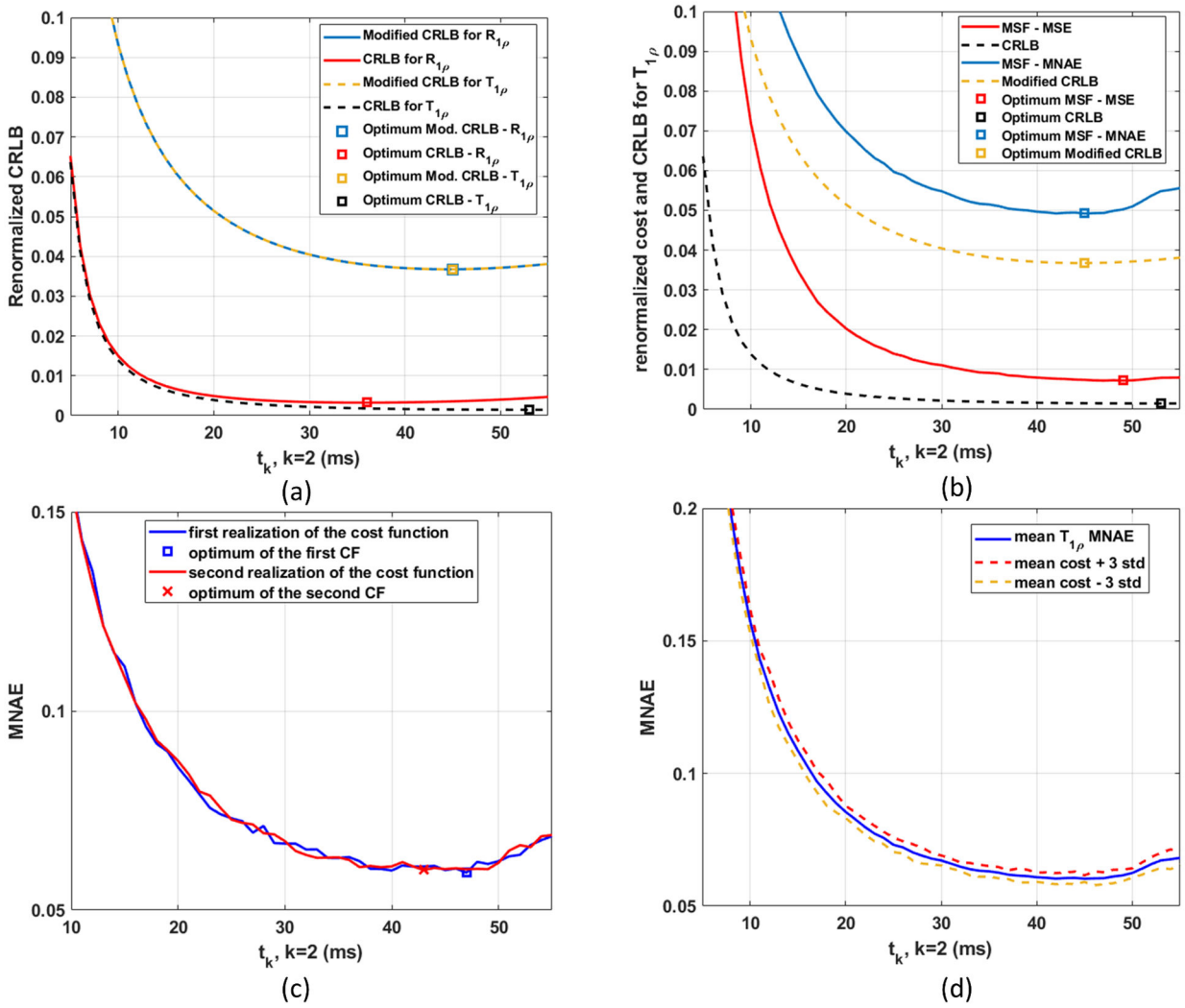


**Figure 2:**

In (a), the comparison of the renormalized costs of CRLB and Modified CRLB when optimizing $T_{1\rho}$ values or $R_{1\rho}$ values, using 2 TSLs, with $\boldsymbol{t} = [t_1\ t_2]^T$, where $t_1$=1 millisecond (ms) and $t_2$ is the optimizing variable. In (b), Modified CRLB has its shape and minimum very close to the MSF-MNAE, while CRLB and MSF-MSE are not so close to one another. In (c) two different realizations of the noisy cost function (for MSF-MNAE) are shown with their corresponding minima. In (d) the mean cost function (averaged from 15 realizations) for MSF-MNAE and the range of ± 3 standard deviations are shown, illustrating where 99.73% of the realizations are expected to be.

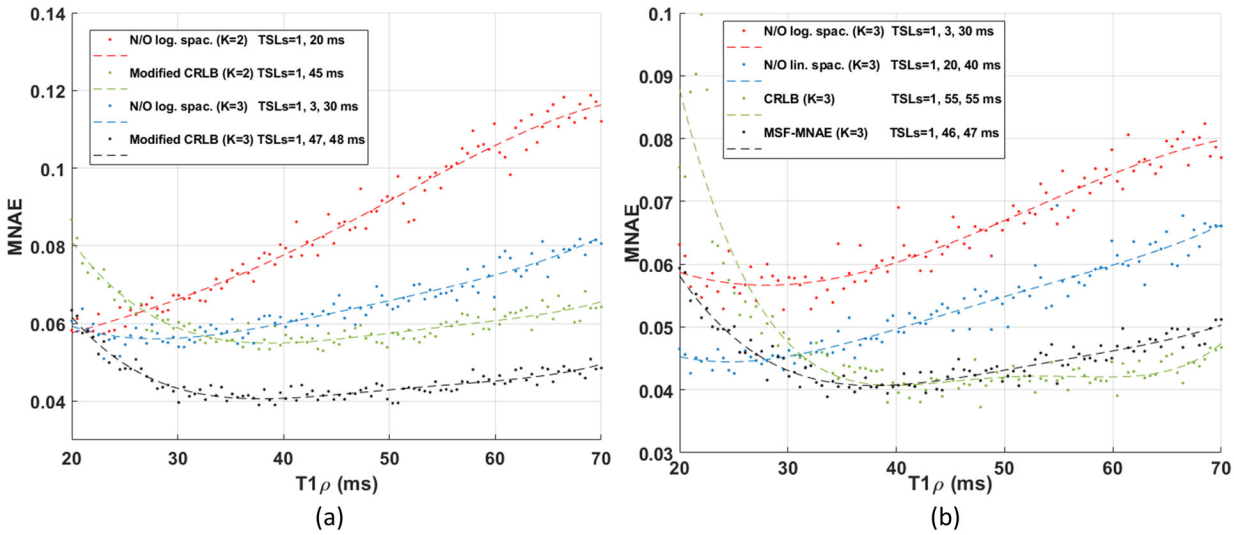


**Figure 3:**

Performance of different choices of TSL in the synthetic experiments with SNR=30 for each expected $T_{1\rho}$ value, measured by MNAE. This curve considers that the measured signal was generated by the specified T1ρ value (in the range of 20 and 70 ms). In (a), increasing K lowers the curve of MNAE. In (b), the optimization finds the best TSL sampling schedules for an expected range of T1ρ values using the same K.

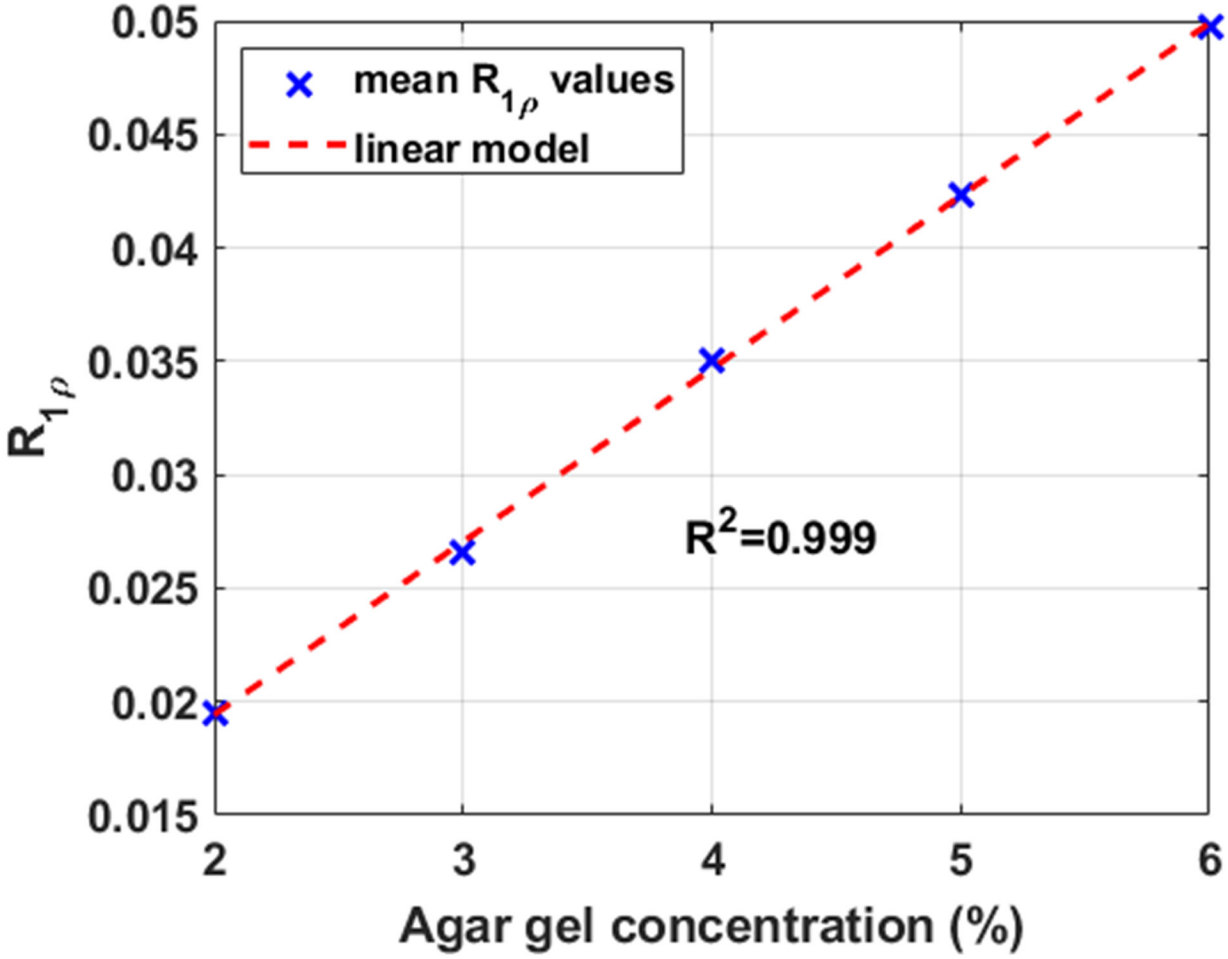


**Figure 4:**
Correlation between $R_{1\rho}$ values and agar gel concentration in the model phantoms.

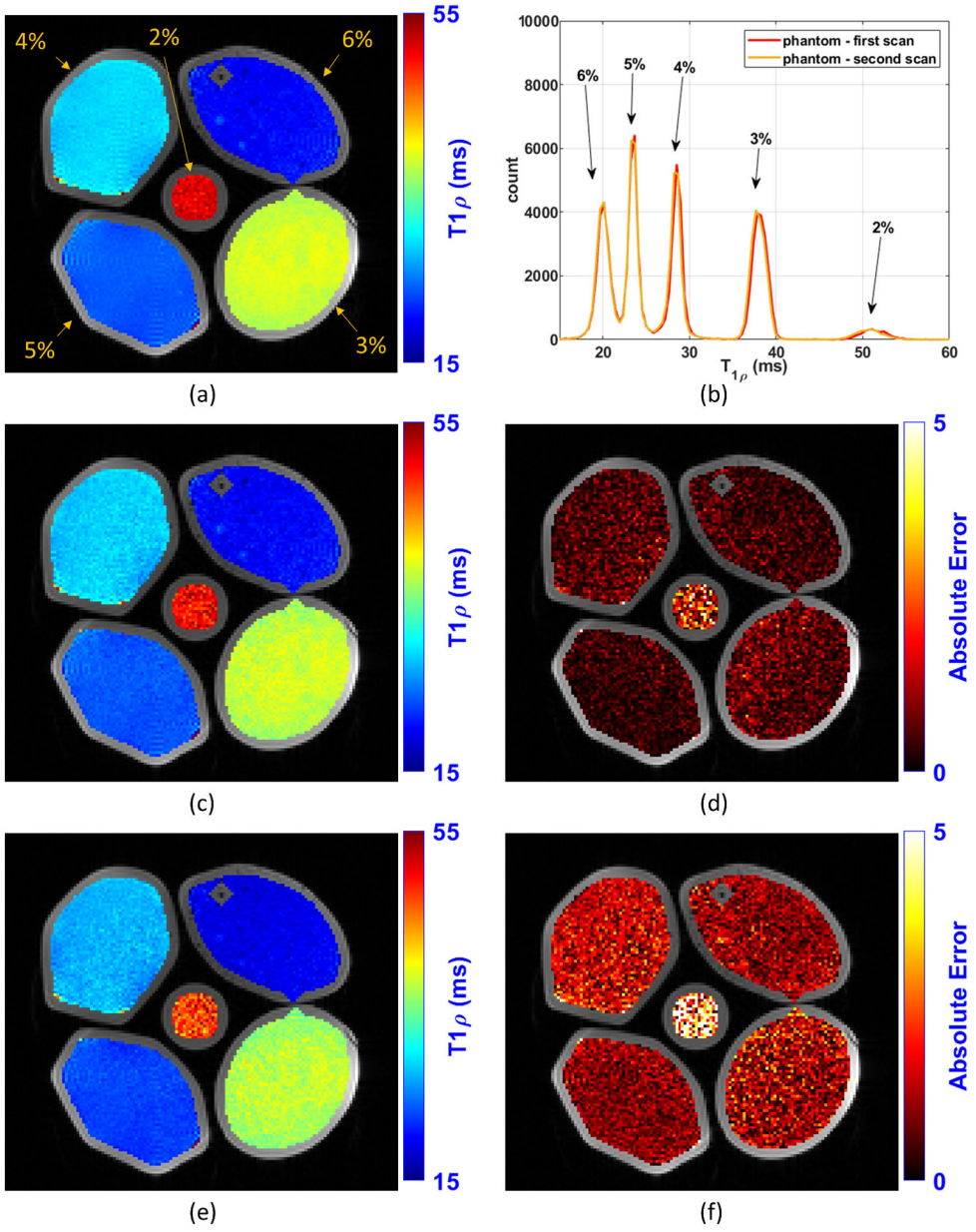


**Figure 5:**

Illustration of the $T_{1\rho}$ maps obtained with the $T_{1\rho}$ agar gel model phantoms experiment. In (a) is shown the reference map obtained using all the 16 TSLs acquired in a phantom scan session (1, 1, 3, 10, 20, 25, 30, 32, 32, 34, 34, 38, 40, 40, 42, 55 ms). In (b) is shown the histogram of the $T_{1\rho}$ values of the phantom (histogram CV=5.9%). In (c) and (d) are shown respectively the $T_{1\rho}$ map and error map obtained with K=2 optimized TSLs: 1, 32 ms (optimal TSLs for Modified CRLB and MSF-MNAE when K=2). In (e) and (f) are shown respectively the $T_{1\rho}$ map and error map obtained with K=2 non-optimized logarithmic scaled TSLs: 1, 20 ms.

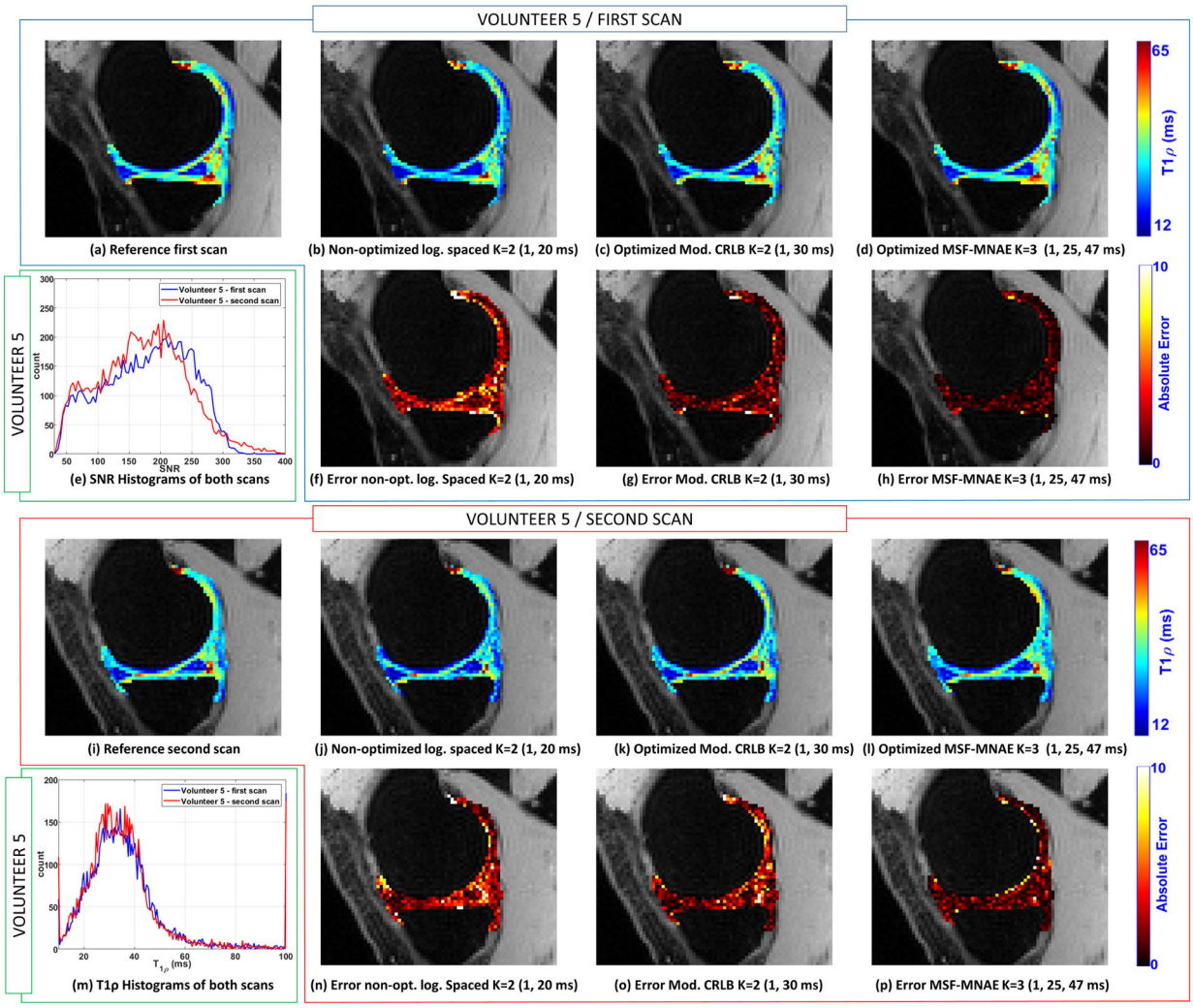


**Figure 6:**

Illustration of the $T_{1\rho}$ maps of the medial cartilage obtained with the volunteer 5. The reference map obtained using all the TSLs (K=15, TSLs=1, 1, 3, 10, 20, 25, 30, 31, 32, 36, 37, 40, 42, 47, 55 ms) from the first scan is shown in (a) and from the second scan in (i). $T_{1\rho}$ map obtained with volunteer 5 in the first scan with non-optimized TSLs (K=2, TSLs=1, 20 ms) is shown in (b), with TSLs optimized for Mod. CRLB (K=2, TSLs=1, 30 ms) in (c), and MSF-MNAE (K=3, TSLs=1, 25, 47 ms) in (d). $T_{1\rho}$ maps of the second scan of the same volunteer are shown in (j)-(l). In (f)-(h) and (n)-(p) the corresponding errors related to the reference are shown. The histograms obtained in the first and second scans are shown in (e) for the SNR (CV=10.9%) and in (m) for $T_{1\rho}$ values (CV=8.6%).

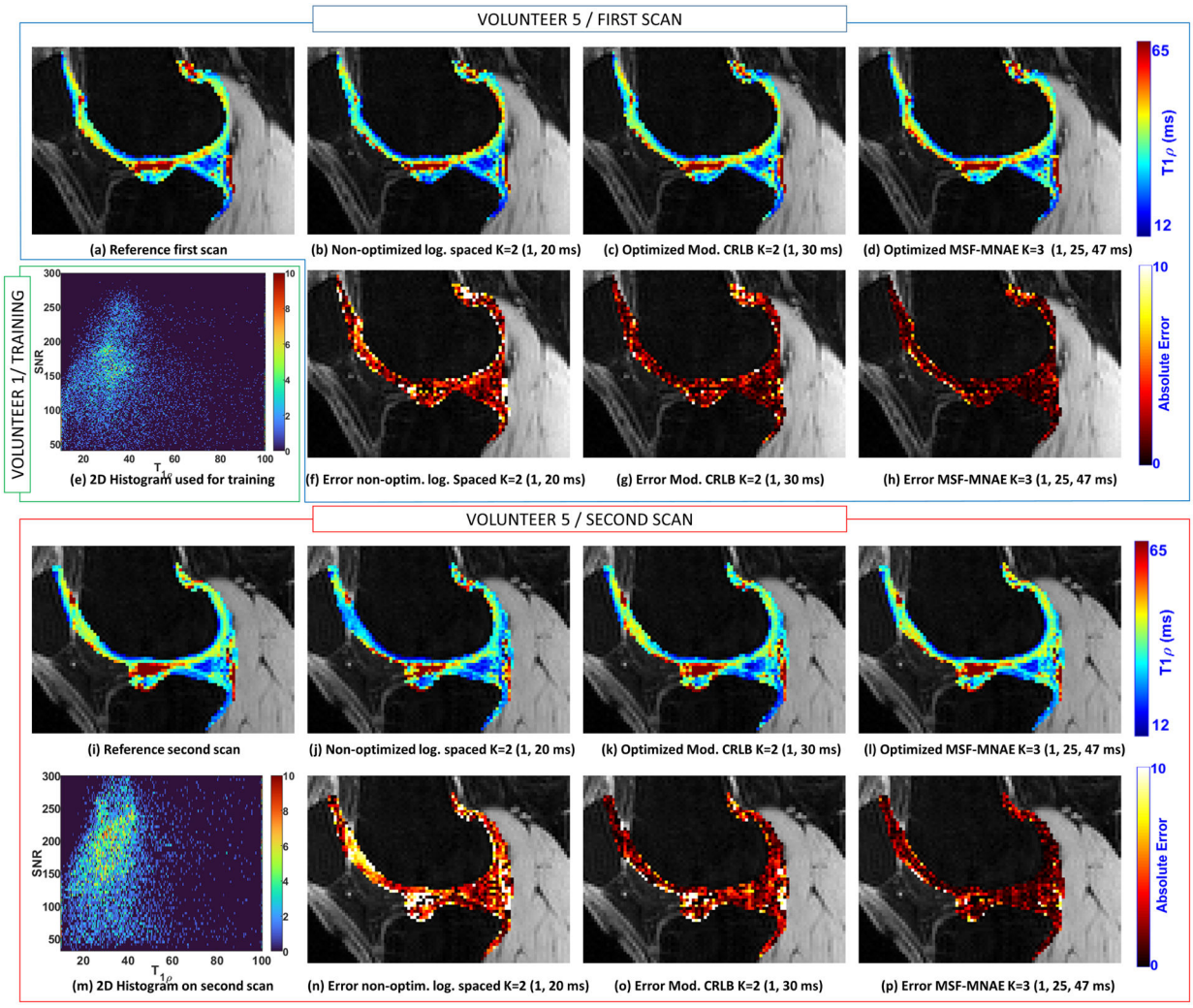


**Figure 7:**

Illustration of the $T_{1\rho}$ maps of the lateral cartilage obtained with the volunteer 5. The reference map obtained using all the TSLs (K=15, TSLs=1, 1, 3, 10, 20, 25, 30, 31, 32, 36, 37, 40, 42, 47, 55 ms) from the first scan is shown in (a) and from the second scan in (i). $T_{1\rho}$ map obtained with volunteer 5 in the first scan with non-optimized TSLs (K=2, TSLs=1, 20 ms) is shown in (b), with TSLs optimized for Mod. CRLB (K=2, TSLs=1, 30 ms) in (c), and MSF-MNAE (K=3, TSLs=1, 25, 47 ms) in (d). $T_{1\rho}$ maps of the second scan of the same volunteer are shown in (j)-(l). In (f)-(h) and (n)-(p) the corresponding errors related to the reference are shown. The 2D histogram obtained with volunteer 1, which was used for the optimization, is shown in (e). The 2D histogram obtained after optimization, with volunteer 5 is shown in (m).

**Table 1:**

Optimized and non-optimized spin lock times, in milliseconds (ms) for the various criteria and sizes K, with SNR=30.

| | | | | | | MNAE | | NRMSE | | | | | | | | MNAE | | NRMSE | |
|---|---|---|---|---|---|---|---|---|---|---|---|---|---|---|---|---|---|---|---|
| **Non-Optimized log. spaced** | | | | | | **NLS** | **ANN** | **NLS** | **ANN** | **Non-Optimized linearly spaced** | | | | | | **NLS** | **ANN** | **NLS** | **ANN** |
| **K=2** | 1 | 20 | | | | 8.6% | 9.3% | 12.6% | 13.3% | **K=2** | 1 | 25 | | | | 7.4% | 7.9% | 10.5% | 11.2% |
| **K=3** | 1 | 3 | 30 | | | 6.6% | 6.9% | 9.0% | 9.5% | **K=3** | 1 | 20 | 40 | | | 5.4% | 5.5% | 7.5% | 7.7% |
| **K=4** | 1 | 2 | 9 | 40 | | 5.8% | 5.9% | 7.9% | 7.8% | **K=4** | 1 | 15 | 30 | 45 | | 4.7% | 4.8% | 6.6% | 6.6% |
| **K=5** | 1 | 2 | 5 | 16 | 50 | 5.2% | 5.2% | 7.0% | 6.8% | **K=5** | 1 | 13 | 26 | 39 | 52 | 4.2% | 4.2% | 6.0% | 5.6% |
| | | | | | | **MNAE** | | **NRMSE** | | | | | | | | **MNAE** | | **NRMSE** | |
| **CRLB** | | | | | | **NLS** | **ANN** | **NLS** | **ANN** | **Modified CRLB** | | | | | | **NLS** | **ANN** | **NLS** | **ANN** |
| **K=2** | 1 | 53 | | | | 6.7% | 6.5% | 7.9% | 7.8% | **K=2** | 1 | 45 | | | | **6.0%** | **6.3%** | 7.6% | 8.0% |
| **K=3** | 1 | 55 | 55 | | | 4.7% | 4.8% | 5.6% | 5.7% | **K=3** | 1 | 47 | 48 | | | **4.5%** | **4.7%** | 5.7% | 5.9% |
| **K=4** | 1 | 55 | 55 | 55 | | 3.9% | 4.1% | 4.8% | 4.9% | **K=4** | 1 | 49 | 50 | 50 | | **3.9%** | **4.0%** | 4.9% | 5.0% |
| **K=5** | 1 | 55 | 55 | 55 | 55 | 3.5% | 3.6% | 4.3% | 4.4% | **K=5** | 1 | 51 | 51 | 51 | 52 | **3.5%** | **3.6%** | 4.4% | 4.5% |
| | | | | | | **MNAE** | | **NRMSE** | | | | | | | | **MNAE** | | **NRMSE** | |
| **MSF-MSE for NLS** | | | | | | **NLS** | **ANN** | **NLS** | **ANN** | **MSF-MNAE for NLS** | | | | | | **NLS** | **ANN** | **NLS** | **ANN** |
| **K=2** | 1 | 49 | | | | 6.2% | 6.3% | ***7.5%*** | **7.8%** | **K=2** | 1 | 44 | | | | ***6.1%*** | **6.3%** | 7.7% | 8.0% |
| **K=3** | 1 | 51 | 54 | | | 4.6% | 4.7% | ***5.6%*** | **5.8%** | **K=3** | 1 | 46 | 47 | | | ***4.5%*** | **4.7%** | 5.7% | 5.9% |
| **K=4** | 1 | 53 | 55 | 55 | | 3.9% | 4.0% | ***4.8%*** | **4.9%** | **K=4** | 1 | 47 | 48 | 52 | | ***3.9%*** | **4.0%** | 4.9% | 5.0% |
| **K=5** | 1 | 54 | 54 | 55 | 55 | 3.5% | 3.7% | ***4.3%*** | **4.5%** | **K=5** | 1 | 46 | 48 | 52 | 54 | ***3.5%*** | **3.6%** | 4.4% | 4.5% |
| | | | | | | **MNAE** | | **NRMSE** | | | | | | | | **MNAE** | | **NRMSE** | |
| **MSF-MSE for ANN** | | | | | | **NLS** | **ANN** | **NLS** | **ANN** | **MSF-MNAE for ANN** | | | | | | **NLS** | **ANN** | **NLS** | **ANN** |
| **K=2** | 1 | 50 | | | | 6.4% | 6.4% | **7.6%** | ***7.8%*** | **K=2** | 1 | 43 | | | | **6.1%** | ***6.3%*** | 7.8% | 8.0% |
| **K=3** | 1 | 51 | 55 | | | 4.7% | 4.7% | **5.6%** | ***5.8%*** | **K=3** | 1 | 43 | 44 | | | **4.6%** | ***4.7%*** | 5.9% | 6.0% |
| **K=4** | 1 | 50 | 55 | 55 | | 4.0% | 4.0% | **4.8%** | ***4.9%*** | **K=4** | 1 | 37 | 52 | 54 | | **3.9%** | ***4.0%*** | 5.0% | 5.1% |
| **K=5** | 1 | 49 | 55 | 55 | 55 | 3.6% | 3.6% | **4.3%** | ***4.4%*** | **K=5** | 1 | 32 | 52 | 54 | 55 | **3.6%** | ***3.6%*** | 4.6% | 4.6% |

**Table 2:**

Optimized and non-optimized spin lock times, in milliseconds (ms) for the various criteria and K=2 and 3 with the $T_{1\rho}$ agar gel model phantoms in a 3T MRI scanner.

| Comparison with the Reference (MNAE and NRMSE), Repeatability (CV), and regression with agar gel ($R^2$) | | | | | MNAE | | NRMSE | | CV | | Regression of $R_{1\rho}$ ($R^2$) | |
|---|---|---|---|---|---|---|---|---|---|---|---|---|
| | | | | | NLS | ANN | NLS | ANN | NLS | ANN | NLS | ANN |
| **Non-Optimized log. spaced** | **K=2** | 1 | 20 | | 5.3% | 4.4% | 6.2% | 5.2% | 1.7% | 1.9% | 0.996 | 0.996 |
| | **K=3** | 1 | 3 | 30 | 2.3% | 2.2% | 3.2% | 2.9% | 1.5% | 1.7% | 0.998 | 0.998 |
| **Non-Optimized linearly spaced** | **K=2** | 1 | 25 | | 3.6% | 3.2% | 4.6% | 4.0% | 1.6% | 1.7% | 0.997 | 0.997 |
| | **K=3** | 1 | 20 | 40 | 2.2% | 2.1% | 2.6% | 2.5% | 1.2% | 1.4% | 0.998 | 0.998 |
| **CRLB** | **K=2** | 1 | 38 | | **2.2%** | **2.3%** | **2.7%** | **2.8%** | **1.6%** | **1.7%** | **0.998** | **0.998** |
| | **K=3** | 1 | 40 | 40 | **2.0%** | **2.1%** | **2.3%** | **2.4%** | **1.3%** | **1.3%** | **0.998** | **0.998** |
| **Modified CRLB** | **K=2** | 1 | 32 | | **2.1%** | **2.0%** | **2.8%** | **2.7%** | **1.6%** | **1.7%** | **0.998** | **0.998** |
| | **K=3** | 1 | 34 | 34 | **1.5%** | **1.5%** | **2.1%** | **2.0%** | **1.2%** | **1.3%** | **0.998** | **0.998** |
| **MSF-MSE for NLS** | **K=2** | 1 | 38 | | **2.2%** | **2.3%** | **2.7%** | **2.8%** | **1.6%** | **1.7%** | **0.998** | **0.998** |
| | **K=3** | 1 | 38 | 42 | **2.0%** | **2.0%** | **2.3%** | **2.3%** | **1.3%** | **1.3%** | **0.998** | **0.998** |
| **MSF-MSE for ANN** | **K=2** | 1 | 40 | | **2.4%** | **2.5%** | **2.8%** | **2.8%** | **1.7%** | **1.7%** | **0.998** | **0.998** |
| | **K=3** | 1 | 34 | 55 | **2.3%** | **2.3%** | **2.3%** | **2.6%** | **1.3%** | **1.4%** | **0.998** | **0.998** |
| **MSF-MNAE for NLS** | **K=2** | 1 | 32 | | **2.1%** | **2.0%** | **2.8%** | **2.7%** | **1.6%** | **1.7%** | **0.998** | **0.998** |
| | **K=3** | 1 | 32 | 34 | **1.5%** | **1.5%** | **2.2%** | **2.0%** | **1.2%** | **1.3%** | **0.998** | **0.998** |
| **MSF-MNAE for ANN** | **K=2** | 1 | 38 | | **2.2%** | **2.3%** | **2.7%** | **2.8%** | **1.6%** | **1.7%** | **0.998** | **0.998** |
| | **K=3** | 1 | 25 | 55 | **1.6%** | **1.8%** | **2.2%** | **2.4%** | **1.3%** | **1.4%** | **0.998** | **0.998** |
| **REFERENCE** | **K=16** | 1, 1, 3, 10, 20, 25, 30, 32, 32, 34, 34, 38, 40, 40, 42, 55 | | | | | | | **0.6%** | **0.7%** | **0.999** | **0.999** |

**Table 3:**

Optimized and non-optimized spin lock times, in milliseconds (ms) for the various criteria and K=2 and K=3 on healthy volunteers in a 3T MRI scanner.

| Comparison with the Reference (MNAE and NRMSE) and Repeatability (CV and ROI CV) | | | | | MNAE | | NRMSE | | CV | |
|---|---|---|---|---|---|---|---|---|---|---|
| | | | | | NLS | ANN | NLS | ANN | NLS | ANN |
| **Non-Optimized log. spaced** | **K=2** | 1 | 20 | | 17.9% | 18.1% | 27.5% | 27.8% | 3.7% | 3.8% |
| | **K=3** | 1 | 3 | 30 | 10.5% | 10.6% | 17.5% | 16.7% | 3.1% | 3.3% |
| **Non-Optimized linearly spaced** | **K=2** | 1 | 25 | | 13.1% | 13.1% | 21.5% | 20.8% | 3.5% | 3.6% |
| | **K=3** | 1 | 20 | 40 | 9.8% | 10.4% | 17.0% | 16.6% | 3.0% | 3.2% |
| **CRLB** | **K=2** | 1 | 42 | | **12.7%** | **12.8%** | **19.8%** | **20.1%** | **2.9%** | **3.0%** |
| | **K=3** | 1 | 36 | 55 | **9.9%** | **9.9%** | **16.3%** | **16.4%** | **2.8%** | **2.9%** |
| **Modified CRLB** | **K=2** | 1 | 30 | | **11.0%** | **11.1%** | **18.2%** | **18.3%** | **2.9%** | **2.9%** |
| | **K=3** | 1 | 30 | 32 | **8.0%** | **8.3%** | **14.2%** | **14.3%** | **2.8%** | **2.8%** |
| **MSF-MSE for NLS** | **K=2** | 1 | 37 | | **12.6%** | **12.7%** | **19.8%** | **19.9%** | **3.0%** | **3.0%** |
| | **K=3** | 1 | 36 | 55 | **9.9%** | **9.9%** | **16.3%** | **16.4%** | **2.8%** | **2.9%** |
| **MSF-MSE for ANN** | **K=2** | 1 | 42 | | **12.7%** | **12.8%** | **19.8%** | **20.1%** | **2.9%** | **3.0%** |
| | **K=3** | 1 | 42 | 47 | **10.0%** | **10.2%** | **14.5%** | **15.6%** | **2.9%** | **2.9%** |
| **MSF-MNAE for NLS** | **K=2** | 1 | 31 | | **10.3%** | **10.7%** | **16.6%** | **16.6%** | **2.9%** | **2.9%** |
| | **K=3** | 1 | 32 | 37 | **7.7%** | **7.9%** | **12.8%** | **12.9%** | **2.7%** | **2.7%** |
| **MSF-MNAE for ANN** | **K=2** | 1 | 32 | | **10.1%** | **10.2%** | **16.5%** | **16.2%** | **2.8%** | **2.8%** |
| | **K=3** | 1 | 25 | 47 | **7.7%** | **7.9%** | **13.9%** | **13.7%** | **2.7%** | **2.7%** |
| **REFERENCE** | **K=15** | 1, 1, 3, 10, 20, 25, 30, 31, 32, 36, 37, 40, 42, 47, 55 | | | | | | | **2.5%** | **2.5%** |